Quantitative MRI study of water distribution during operation of a PEM fuel cell using Teflon® flow fields

Zachary Dunbar, Richard I. Masel *

Department of Chemical and Biomolecular Engineering, University of Illinois, 600 S Mathews, Urbana, IL 61801, United States

Abstract

Water management remains a leading challenge in the implementation of small polymer electrolyte membrane (PEM) fuel cells for portable electronic applications. At present there are many excellent models for the distribution of water within PEM fuel cells, but little quantitative data on the water distribution that can be compared to models.

In this paper magnetic resonance imaging (MRI) is used to examine the water distribution in the flow fields of an operating PEM fuel cell. While previous workers have used MRI to do qualitative measurements of the water distribution, we use MRI to quantitatively measure the water distribution for the first time. We find that even with Teflon® flow fields the GDL is so hydrophobic, that water is drawn away from the cathode GDL and accumulates at the bottom of the flow field. The flow pattern in the flow field seems to be wavy-stratified flow rather than plug flow as previously supposed. Additionally, we find that water is transported from the cathode to the anode. Thus, diffusional forces and hydrophobic capillary pressures appeared to dominate electroosmotic forces, at low current densities.
© 2007 Elsevier B.V. All rights reserved.

Keywords: MRI; Fuel cell; Water; PEM; Transport

1. Introduction

Water management is still a major challenge in PEM fuel cells [1,2]. There are many excellent models of the water distribution as reviewed by and Cheddie and Munroe [3], Ma et al [4] and Wang [5] but there is much less quantitative data. Neutron scattering has provided two-dimensional pictures of the water in fuel cells [6–11], but extensions to three dimensions, and quantification of the spacial data has been difficult. Magnetic resonance imaging has often been used to examine water motion within a proton conducting membrane [12–38] and a few studies MRI have been done to examine the water in the membranes of operating fuel cells. [17,18,23,36–39]. However, no one has measured the spacial distribution of water in the flow fields in a quantitative way.

In this paper we use MRI to obtain the first three-dimensional, quantitative images of the water distribution in an operating PEM fuel cell. We found surprises. The flow regime in the flow fields is not as previously supposed and there is more water transport from the cathode to the anode than previously assumed.

2. Experimental design

All of the measurements were done in a small fuel cell, with Teflon® flow fields shown in Figs. 1 and 2. The fuel cell was mounted in 14.1 T widebore magnet, and MRI images were accumulated as a function of time. Our approach was similar to previous investigators [39], but a higher field magnet to improve resolution. We also added reference capillaries so we could quantify the results.

2.1. Fuel cell schematic

Due to the strong magnetic field present, certain modifications were necessary to the fuel cell to insure compatibility with the magnet. Teflon® was used as the material for the flow fields, instead of graphite, due to the magnetically inductive nature of graphite. Pure gold was used as the current collector, due to its
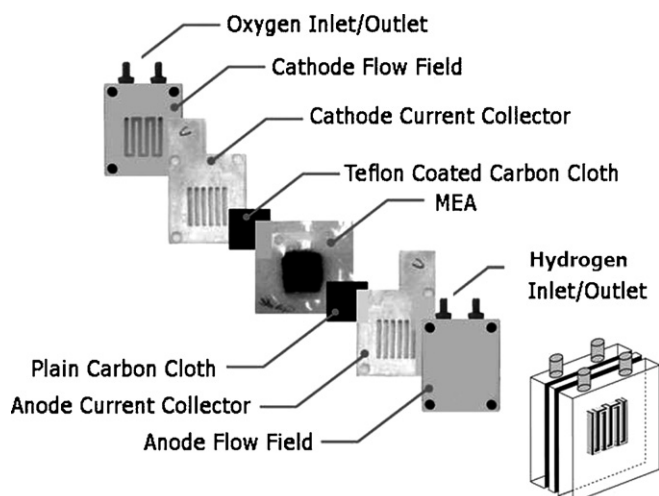
Fig. 1. Exploded view of the fuel cell used in this study. Both anode and cathode flow fields are composed of Teflon®. Current collectors are solid gold. Anode GDL is untreated carbon cloth. Cathode GDL is Teflon® treated carbon cloth. Fuel cell is compressed together using nylon screws.

high electrical conductivity, and lack of ferromagnetic properties. The small relative amount of gold used limited the noise caused by magnetic induction inside the gold. The flow field channel width was 1 mm, and the channel depth was 3 mm.

The MEA was fabricated in the following manner. Nafion 115 (Ion Power) was used as the PEM. Catalyst ink, consisting of platinum black (Alfa Aesar) and Nafion® solution (Ion Power), was applied to each side of the Nafion® using a 'direct paint' technique [40]. The loading on both the cathode and anode was $2 \, mg \, cm^{-2}$. The total surface area of the anode and cathode were both $1 \, cm^2$. The GDL's used were Teflon® treated carbon cloth
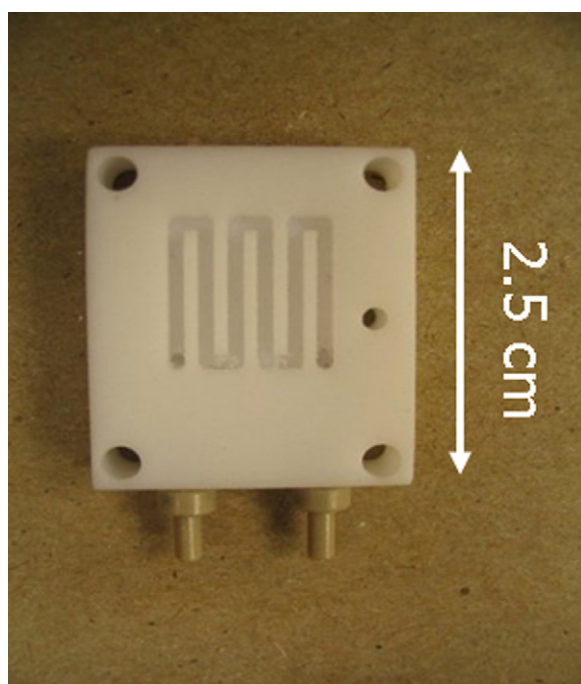

Fig. 2. Frontal view of a Teflon® flow field used in this study. Channels are 1 mm wide and 3 mm deep, in serpentine pattern.

for the cathode, and plain carbon cloth for the anode (E-tek). The fuel cell schematic is shown in Fig. 1.

A unique feature of this fuel cell was the use of water filled capillaries, attached to the fuel cell flow fields, to act as calibration standards for analyzing the water signal. Capillaries were attached to the outside of the flow field using melted capillary wax. Three capillaries were used, one along each of the principal axes of the assembled fuel cell.

Twisted pair wire was used to carry the current and voltage a safe distance from the MRI magnet, were they could be measured and controlled by using multimeters (Fluka) and a variable resistor (Allied Electronics). Reactant gas for the fuel cell was provided by hydrogen and oxygen cylinders housed outside the magnetic field, and controlled by mass flow controllers. Vinyl tubes carried the gas to the fuel cell.

2.2. MRI operation and water quantization information

The fuel cell was placed vertically inside the imaging scanner (Oxford Instruments, Abington, UK) equipped with a Unity/Inova console (Varian, Palo Alta, CA), operating at 14.1 T with a bore of an internal diameter of 5 cm. Varian transmitter/receiver quadrature RF coil was used with an internal diameter of 3.0 cm. T2-weighted coronal (along a vertical axis) 2D sections were acquired using a Spin-Echo multi-slice pulse sequence. The images were acquired slice by slice, with a 0.5 mm gap.

The acquisition time for each sequence was 4 min and 19 s. The repetition time was 1000 ms, and echo time 10 ms. Two transients/averages were taken. The spectral width was 71 kHz, and the field of view was 5.0 cm × 2.5 cm. Each voxel represented a volume 138 μm high by 138 μm wide by 200 μm thick. Water intensity signal was recorded for each voxel. The data was stored to a data file that would be analyzed using MATLAB software.

Water was quantized through use of glass reference capillaries, with an internal diameter of 0.9 mm. The capillaries were oriented along the three Cartesian coordinate planes of the fuel cell, and filled with Millipore® water prior to being placed in the fuel cell. The capillaries were sealed with wax to prevent evaporation during testing. Water content quantization calibrations were initially conducted by filling the flow fields with pure water (and plugging the input/output lines) and comparing signals with that of the capillaries. The water signals per voxel for both trials were within experimental error of each other, and the capillaries were deemed accurate enough for quantization efforts.

Temperature variations between capillary water and water generated in the flow field could lead to variations in the signal, but variations were assumed to be small, and were not characterized in this work.

It must be noted that there was some ambiguity between were the voxels of data generated by the MRI were located spatially, and the exact interface of the Nafion®, catalyst layer, GDL and flow field. This introduces some error into the water concentration data, due to the averaging of water signal over the entire voxel. It is thought that the relatively small voxel size limits this phenomenon.

One aspect of the MRI images should be noted. Due to the angle that the MRI acquires the 'slices' of the fuel cell, not all areas of the fuel cell are visible in every slice. The visible areas of the fuel cell were dependent on were the MRI was focused. In the MRI images presented below, areas of the fuel cell that were not in focus are covered with a semi-transparent "mask" to aid in visualization by the reader.

2.3. MATLAB data analysis

MATLAB software was used for two purposes. The first use was to generate MRI images for the data file generated by the MRI machine. Contrast, brightness and relative noise levels were all adjustable. These images produced were saved in a bitmap data format to minimize data loss.

The second important feature of the MATLAB software was the ability to quantify water content data. Each picture 'slice' the MRI took generated a data file that was stored in a matrix format. Columns and rows corresponded to the horizontal and vertical directions in physical space. The value at each point in the matrix corresponds to the water intensity signal generated by the MRI.

The MATLAB program read in the matrix, and calculated the average signal intensity in the reference capillary. This was assumed to be the intensity given by pure water. Since the volume of the capillary is known, one can then correlate the intensity given by the MRI to a given mass of water occupying that volume.

Next, the water intensity is examined in the rest of the fuel cell. This intensity was divided by the area of the fuel cell, to generate an average intensity. This average intensity was compared to the intensity of the reference capillary. This generated a ratio of intensities, which could then be converted to the mass of water present in each MRI slice.

MRI images were collected of the operating fuel cell. Each MRI image represents the water content in a 200-μm thick "slice" of the fuel cell. Images were taken from two different angles; a front view, Fig. 2, as well as a profile view profile which was rotated 90° from the front view.

To aid the reader in understanding precisely where the MRI water signal was located spatially, the MRI signal was superimposed onto a digital photograph of the fuel cell.

2.4. Experimental conditions

The fuel cell was held at 200 mA cm^{-2} constant current at all times. The fuel cell was operated for 1 h before any images were acquired, in order to reach a steady state water concentration. The anode gas was dry hydrogen, with a flow rate of 40 sccm, while the cathode was dry oxygen, at 40 sccm. The fuel cell was operated at room temperature, approximately 18 °C.

3. Experimental results

3.1. The cathode flow field region

Fig. 3 shows an MRI image of the cathode side of the flow field. Several features of note are highlighted. First, a large
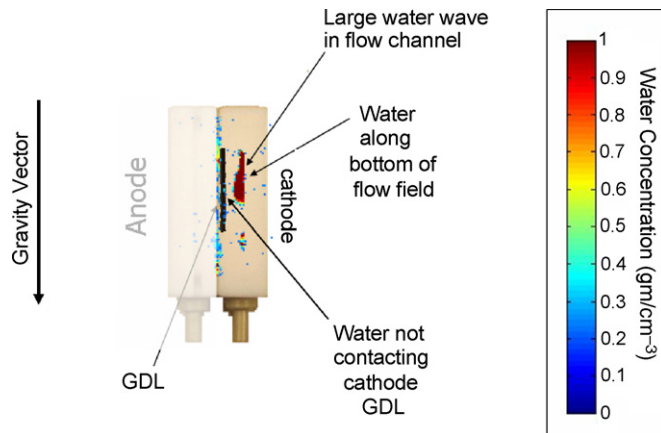

Fig. 3. Profile view of the water concentration in the cathode flow field. A large water wave occupies the bulk of one flow channel. In all figures displaying an MRI signal, the signal is superimposed onto a photograph of the Teflon® flow fields to aid the reader in visualizing the spatial water distribution. Additionally, an image of a gas diffusion layer is superimposed on top of the MRI signal to aid in visualization of the location of the GDL. The fuel cell was held at 200 mA cm^{-2} constant current at all times. The fuel cell was operated for 1 h before any images were acquired, in order to reach a steady state water concentration. The anode gas was dry hydrogen, with a flow rate of 40 sccm, while the cathode was dry oxygen, at 40 sccm.

amount of water was observed in the flow channels of the flow field. Most of the water sits in a single large mass in the bottom of the flow field. The mass was quite large, accounting for the majority of the water signal present in this image. It should be noted that the water wave is not contacting the surface of the cathode GDL (Teflon® coated carbon cloth), but instead was observed along the bottom wall of the flow field, away from the MEA and GDL. This was somewhat surprising, since the flow field was made of hydrophobic Teflon®. It was thought this hydrophobicity in the flow field might 'hold' the water close to the GDL surface, and inhibit mass transfer of oxygen. But interestingly, the Teflon® appears to be 'pulling' the water down to the bottom of the flow channel. Additionally, there was a thin coating of water all along the bottom of the cathode flow field, even in areas without a water wave. It was theorized that the Teflon® coated carbon cloth might be more hydrophobic than the Teflon® flow field, and thus driving the water down into the channel bottom.

In a larger way, the image in Fig. 3 is not quite as we had expected. In previous studies, movies of the water motion in flow fields make it look like slugs of water are moving in the flow channels. However, the image in Fig. 3 does not look as expected for slug flow; see Fig. 4. Instead the figure is as expected for wavy-stratified flow. A series of consecutive MRI images show waves of water moving slowly through the flow field. The relative size and shape of an individual wave, as well as the spacing between multiple waves lead us to believe we are watching the slow propagation of waves through the flow channels, not a new wave that has quickly displaced the old wave, during the 4 min 19 s MRI acquisition time. The waves are transported by friction with the moving gas, but the wave moves at a much lower speed that the air. This is in contrast to slug-flow where the velocity of water and air would be the same. Fig. 5 is the same area of the
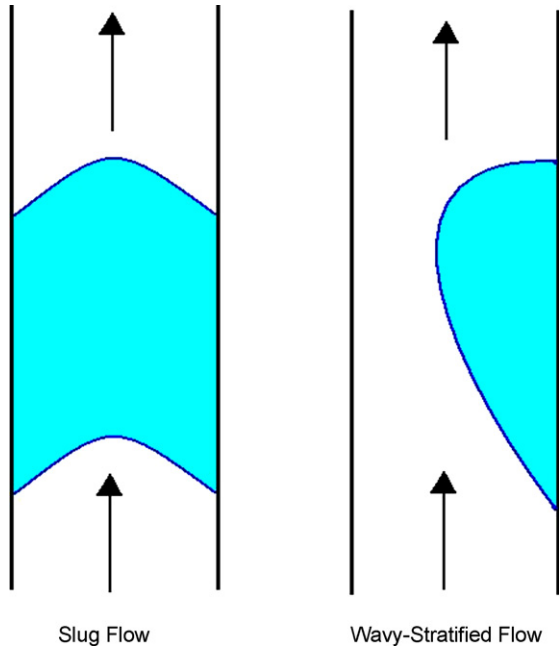
Fig. 4. A diagram of the profile of a water slug and a water wave.

Fig. 5. Front view of cathode flow field. Multiple water waves are visible at various points in the flow field.

fuel cell as Fig. 3, but simply rotated 90°. Several water waves were observed. It was observed that they are moving through the flow field flow channels, along the serpentine path. This angle does not convey any 'depth' data, but when Fig. 3 is taken into consideration, it was clear that the waves were not contacting the GDL, and there was a gas layer present between the water waves and the GDL surface. The key message from Fig. 5 is that the waves do not have a fixed wavelength as one would expect for classic Jeffrey's waves. Instead one observes a variety of wavelengths and wave spacing, as one might expect for roll waves [41].

Fig. 6 is a spatial water content graph, relating water content to the distance from the MEA. At distance 0, the water signal came from the water-rich Nafion® membrane in the MEA. Water content then dropped sharply as distance was increased away from the membrane. Around 1 mm away from the MEA,
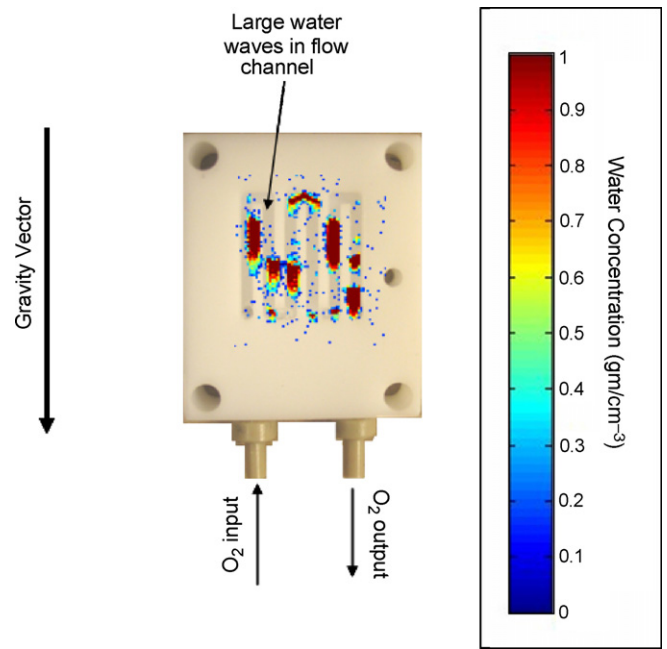
the tip of the water wave was observed, stretching over one mm in thickness. Near the bottom of the flow field, the water content spikes again, to its highest concentration yet. This was a combination of the bottom of the water wave, and of the general wetting of the bottom of the flow field channels described earlier.

This illustrates that the Teflon® flow field is channeling water down to the bottom of the flow field, away from the GDL surface.

3.2. The cathode GDL and MEA region

In the next series of images, the cathode GDL region was highlighted as the area of interest.

Since the MRI has been refocused on the GDL region, the water waves are no longer visible, but are still present physically in the fuel cell.
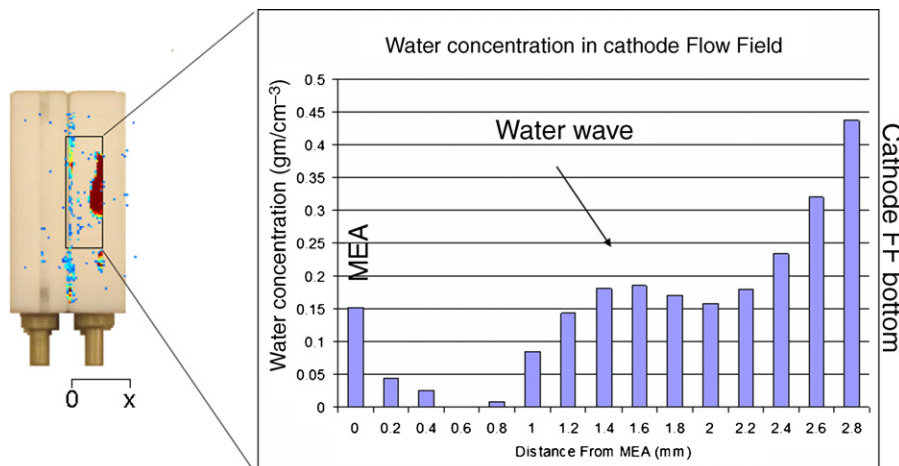

Fig. 6. Average water concentration distributions of the cathode flow fields at various distances from the MEA. Concentration is highest along the back wall of the cathode flow field.
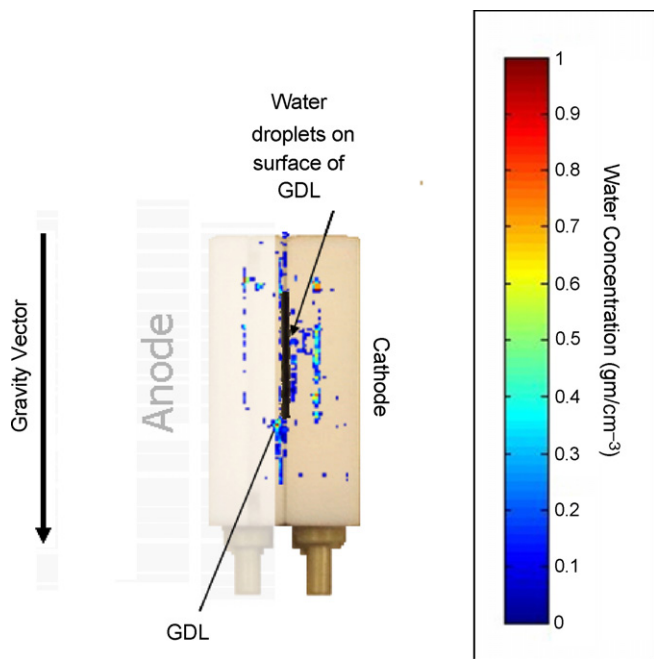
Fig. 7. Profile view of the water concentration in the gas diffusion layer of the cathode. A layer of water is observed on the side of the GDL facing the flow field and the reactant gas stream.

Fig. 7 shows a clear gap between the water rich MEA sheet, and water droplets present on the GDL surface. This 'gap' is an effect of the carbon cloth used as the GDL. The magnetically inductive qualities of carbon prevent the MRI from acquiring a useable signal from this region of the fuel cell, resulting in an 'empty' region of water signal. Fig. 8 represents the same MRI signal, but has a picture of the GDL superimposed to add clarity for the reader.

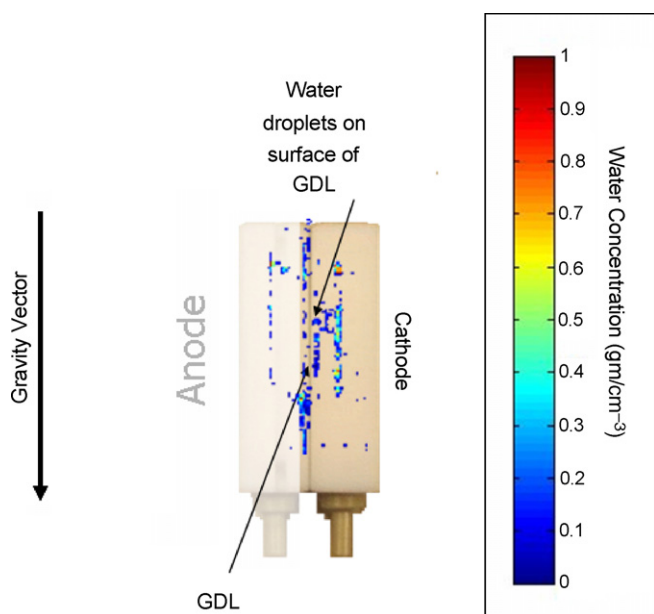There are observable water droplets on the surface of the GDL. Due to the ambiguity of how the voxels generated by the MRI overlap with the physical dimensions of the carbon cloth GDL, some caution must be used when interpreting the results, however it appears that the presence of the water droplets indicate that water was diffusing through the Teflon® treated GDL. Based on the previously discussed figures, much of this water appeared to be quickly transported into the moving water waves. The water content on the GDL surface was small relative to the amount of water in the water waves deeper in the flow channels. We suppose that the droplet transfer process is very similar to the droplet transfer process often observed in wavy-stratified flow in pipes, where lift forces entrain the water droplets and carry them into the moving water waves.

The amount of water present on the GDL surface was virtually constant versus time (after the 1 h equilibration time given at the start of the experiment). The relatively small amount of water content on the GDL surface, as well as the fuel cell performance data appear to indicate that no flooding is occurring at these reaction conditions.

The front view of the fuel cell presented in Fig. 9 further illustrates the water droplets present on the surface of the GDL. The distance from the MEA was not apparent from this angle, but the moderate amount of dispersed water droplets were visible.

The distribution of water was somewhat uniform, although most of the water appeared to be located at the top of the GDL surface. Additionally, it appeared that more water began to accumulate on the GDL as the reactant gas progressed from inlet to outlet.

The spatial water content data is shown in Fig. 10. It demonstrates quantitatively what has been observed in the previous MRI images. A large amount of water was present in the MEA, due to the water present in the Nafion®. The bulk of the water in the Nafion® originated from the oxygen reduction reaction, due to an observed increase in water content once the fuel cell was operated at constant current, compared to preliminary images of

Fig. 8. Profile view of the water concentration in the gas diffusion layer of the cathode, without a superimposed image of the GDL.
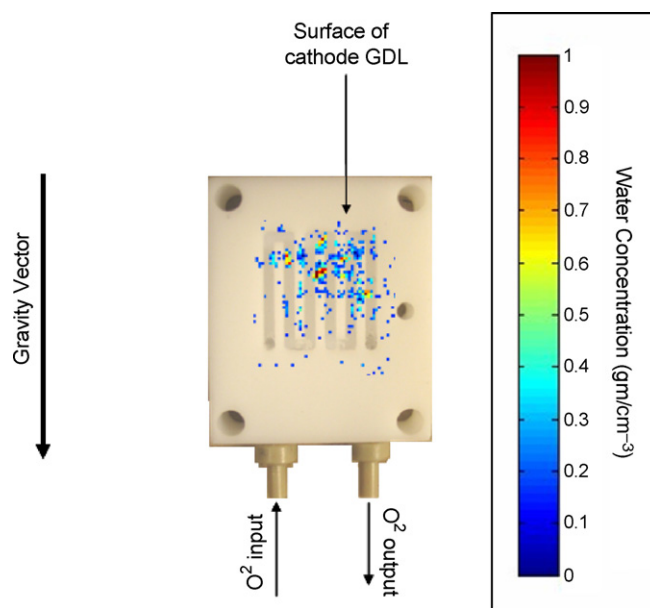

Fig. 9. Front view of the top of the gas diffusion layer on the cathode side of the MEA. Dispersed water droplets are visible across GDL surface facing the flow field.
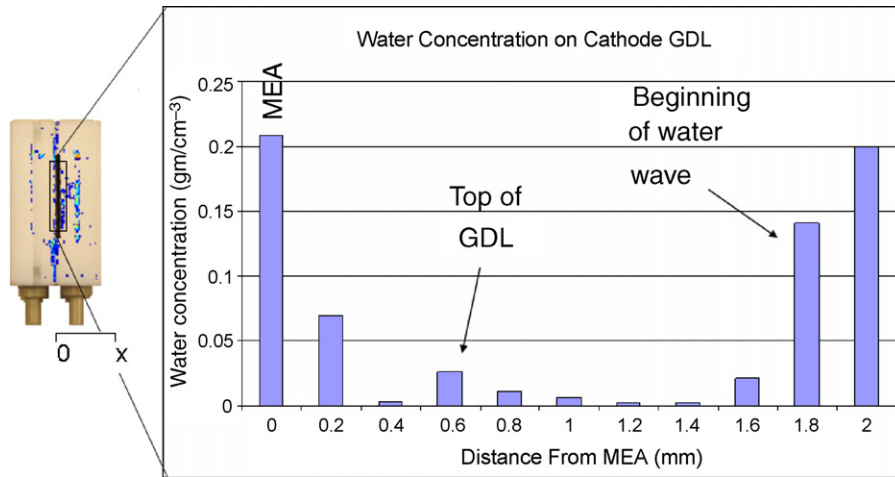
Fig. 10. Average water concentration distributions of the cathode GDL at various distances from the MEA.

the fuel cell at open cell potential. As distances increased from the MEA, the water content dropped sharply, due to the lack of water signal inside the cathode GDL. A spike of water was observed 0.5 mm from the MEA surface, which coincides with the water on the surface of the GDL.

After the water spike, the water content quickly drops again, due to the lack of water present in the flow channels in the immediate vicinity of the GDL.

3.3. Water in anode flow fields

Fig. 11 illustrates the profile view of the anode flow field region. No water is produced in the anode region, nor is the input gas humidified. There are three primary forces at work in the region to determine water content; diffusion, capillary backpressure and electroosmotic drag.

Water produced on the cathode can diffuse from the high water concentration region of the cathode to the low water concentration region of the anode. In the absence of any charge transfer, this is the only direction of water movement possible. However, when charge is being transferred, movement of

protons from the anode to the cathode though the Nafion® induce an oppositional force, electroosmotic drag, which can 'pull' water along with the protons. This can cause water to move from the anode back to the cathode. Additionally, the hydrophobic cathode GDL can exert a capillary back pressure on water moving towards the cathode, driving it back to the anode.

The image above shows a relatively large amount of water along the back wall of the anode flow field. It appeared that the Teflon® flow fields were acting to 'pull' water away from the anode GDL. Much like in the cathode region, the exact cause for this was not well understood, but might be caused by variable hydrophobicities of the Teflon® in different areas of the channel.

Since there was water present in the anode flow field, it was clear that diffusion and hydrophobic GDL induced backpressure play a significant role in the distribution of water. These are the only forces that can transport water into this region of the fuel cell. Although electroosmotic forces were also at work, they appear to have been dominated by the other two forces, at least at cell currents of $200\,\mathrm{mA\,cm^{-2}}$. If the electroosmotic forces
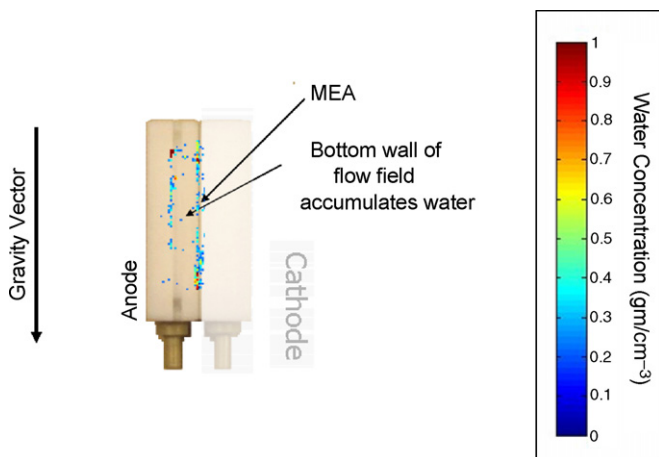

Fig. 11. Profile view of the water concentration in the anode flow field. The majority of the water is along the back wall of the flow field.
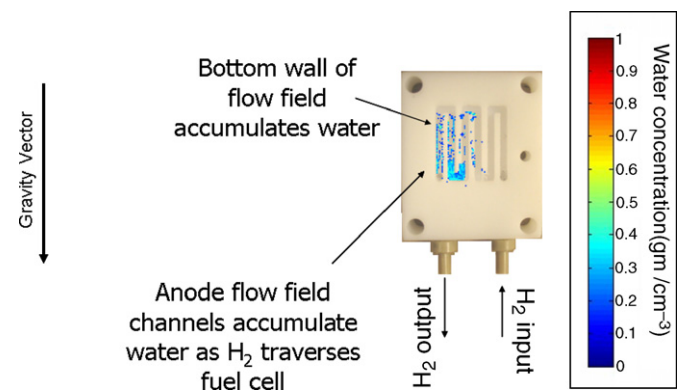

Fig. 12. Front view of anode flow field. Water is visible along the bottom of the flow field. Water concentration grows as the reactant hydrogen travels through the flow channels, indicating it is picking up water diffusing through the membrane from the cathode.
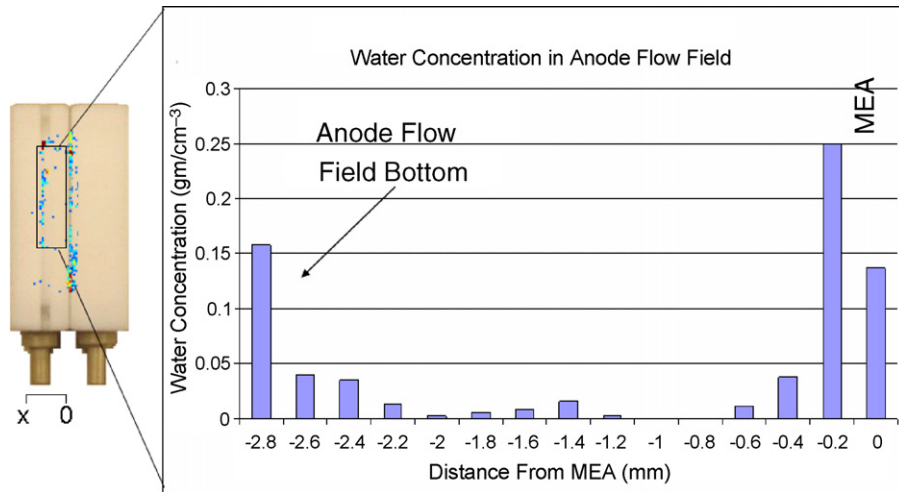
Fig. 13. Average water concentration distributions of the anode flow field at various distances from the MEA. The bulk of the water is along the back wall of the anode flow field.

were stronger, one would expect a 'dry' anode, with little water signal. This is not what was observed.

Another angle of the anode flow field reveals further insight to the water transport within the fuel cell, seen in Fig. 12. The input stream to the fuel cell was dry hydrogen. The gas gradually accumulated water as it traversed the length of the serpentine flow channels. The only possible source of this water was from water generated at the cathode, transported via diffusion and capillary backpressure through the membrane to the anode side.

It was therefore clear, that at $200 \, mA \, cm^{-2}$, the diffusional and capillary backpressure, not electroosmotic, forces are the dominate forces when determining the direction of water transport on the anode.

The water content in the in the anode flow field shown in Fig. 13, was divided into two main areas. First, the MEA contained a large amount of water, due to the hydrated Nafion® membrane. The bulk of the flow field was devoid of much water, as was expected, since all water generation occurs on the cathode

side of the fuel cell. A surprisingly large amount of water was found on the bottom of the anode flow field. In a similar fashion to the cathode flow field, there appears to be a wicking action occurring, due to the Teflon® flow field. This was transporting the water to the bottom of the anode flow field.

3.4. Water in anode inlet/outlet tubes

The final region of the fuel cell imaged was the inlet and outlet tubes of the anode flow field, shown in Fig. 14. A large amount of water was present in the anode exhaust tubes. Since the water had to originate in the cathode, this offered further evidence that transport of water from the cathode was significant.

The front view shown in Fig. 15 provided more information about water transport. It was quite clear that the hydrogen stream coming into the cell was dry, since no water signal was observed. However, the outlet tube was filled with water, providing further evidence of the strength of the diffusional and capillary forces, relative to any electroosmotic forces present.

The water content graph seen in Fig. 16 confirms the previous observations. Significant water was present in the MEA,
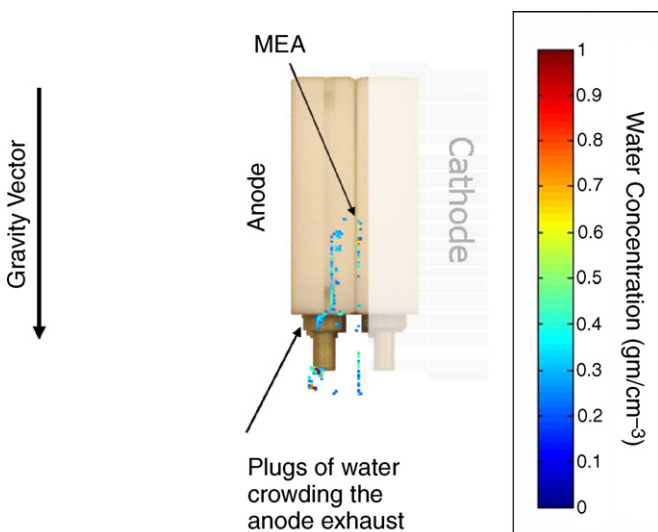

Fig. 14. Profile view of the water concentration in the anode input/output tubes.
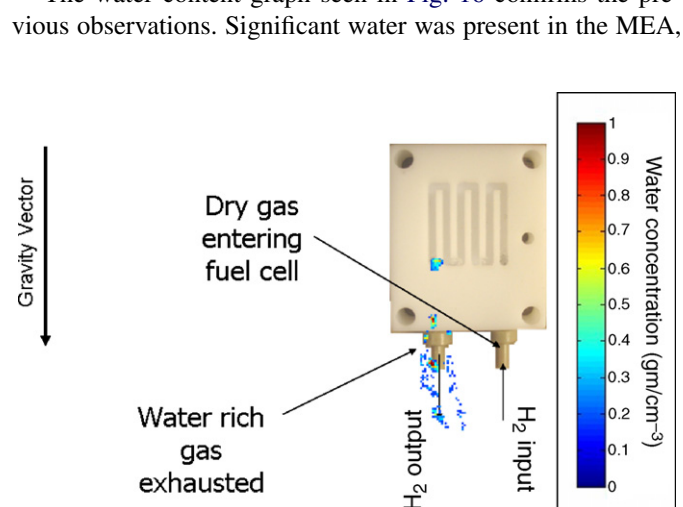

Fig. 15. Front view of the anode tubes. Small waves of water can be observed near the anode exhaust tube, indicating water has diffused from the cathode.
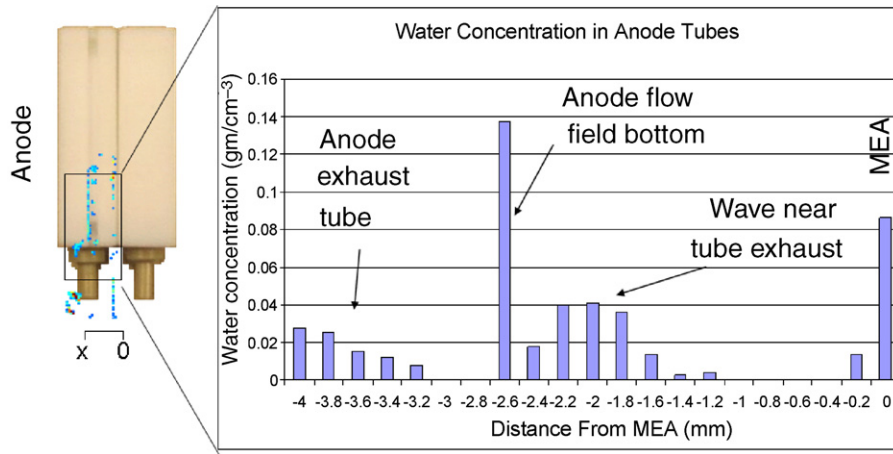
Fig. 16. Average water concentration distributions of the anode tubes at various distances from the MEA.

due to the Nafion® membrane. Water was still observed on the bottom of the Teflon® flow field. Little water was seen inside the bulk of the flow field, however. Additionally, large waves of water are seen in the anode outlet tube. Therefore, not only were diffusional and capillary forces large, they were large enough to cause water waves on the same order of magnitude in size as those observed in the cathode flow field.

3.5. Overall water distribution

The water content of each of the three primary regions of the fuel cell were calculated and presented in Fig. 17. The regions of the fuel cell were defined as the cathode region (consisting of cathode flow field, and GDL), the MEA, and the anode region (containing the anode flow field and GDL).

Unsurprisingly, the cathode contained the most water, at 61%. Due to the oxygen reduction reaction generation of water and the water waves observed in the MRI images, this was the expected result. The MEA contained the second most amount of water. The anode region contains the least amount of water. Most of this water was distributed along the bottom of the flow field. It should be noted that the water accumulating in the anode exhaust tubes were not taken into consideration when determining the water distribution inside the fuel cell itself.
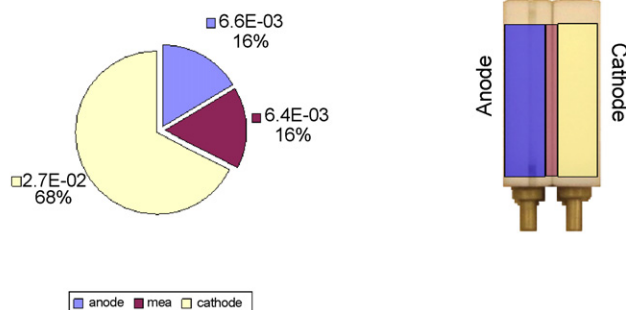

Fig. 17. Overall water content in the anode flow field region, MEA region, and cathode flow field region of the fuel cell.

4. Discussion

The results here were largely as we expected, but there were a couple of key differences. First, we found that the flow pattern in the flow fields was wavy-stratified flow rather than slug flow. After we did the experiment, and looked in the literature, we found that we should have not been surprised. Akbar and Ghiaasiaan [42] and Wallis and Dodson [43] have done extensive studies of air/water flows in pipes and have developed criterion for the transition between wavy-stratified flow and slug flow. Generally one observes slug flow only when the volumetric flowrate of water is within and order of magnitude or so of the volumetric flowrate of the air. All of our data were taken under conditions where wavy-stratified flow would be expected according to the models of Akbar and Ghiaasiaan [42] and Wallis and Dodson [43] The physics in flow fields is different than in Akbar and Ghiaasiaan [42] and Wallis and Dodson [43]. In particular the restoring force is surface tension not gravity and the stratification is driven by a difference in surface tension between the MEA and the flow field walls. Still, our data clearly demonstrates that we have water waves, not slugs in the flow field. It should be noted that our deep flow field channels may play a role in the formation of wavy-stratified flow, compared to a shallower channel depth. However, according to the models of Akbar and Ghiaasiaan [42] and Wallis and Dodson [43], the cell should maintain the wavy-stratified flow regime even at much shallower depths (sub-500 μm)

We believe that the observation of wavy-stratified flow rather than plug could have some important implications to our understanding of fuel cells because the mechanism of water transport is different in the two cases. In slug flow, drops builds up on the surface of the MEA until a slug of water comes by and sweeps the droplets away. In contrast, in wavy-stratified flow, the water droplets can be removed via the lift that is created when the air blows over the curved surface of the drop. Generally, small droplets do not have enough lift to be removed. However, once the drop is large enough, lift forces will carry the drops off of the MEA. As a result, on can view the water transport as a process where water droplets grow until they are large enough to be lifted off of the surface, instead of a process where water

droplets of all sizes are swept away when a slug moves over the surface. We see this process most clearly on the anode, where there are no water waves, yet the water drops are removed from the surface. Then a new water drop grows at almost the same place.

The other key difference between slug flow and wavy-stratified flow is that the water velocities are much lower in wavy-stratified flow than in plug flow. In slug flow, the water slug goes all of the way across the flow channel, so in order for the air to move, the air has to push the slug along. The result is that the water is accelerated until the water velocity equals the air velocity. In contrast with wavy-stratified flow, the air can flow through the gaps between the waves and the MEA. As a result, the water can move much more slowly than the air. In our experiments, the air velocity in the flow fields was about $0.2\,\mathrm{m\,s^{-1}}$ while the liquid velocity was less than $0.001\,\mathrm{m\,s^{-1}}$, for example. The moving air exerts a drag force on the liquid. However, the drag force is much smaller than the body force in slug flow. As a result water can accumulate at dead zones in the flow field. That water can produce freeze damage. Notice that water accumulates near the bends in the flow field in Fig. 5 and the water is not swept away when a wave moves past. This occurs because there is insufficient drag to pull all of the water out of the bend. These small places are spots where there is likely to be freeze damage if the fuel cell were frozen.

5. Conclusions

In this work, MRI technology was used to obtain a three-dimensional quantitative water distribution profile inside an operating fuel cell.

It was found that the Teflon® flow fields enhance water transport away from MEA and GDL. Due to the hydrophobic nature of the Teflon® flow fields, it was expected that the water might be trapped on the GDL surface, but instead it was actively pulled to the bottom of the flow field apparently by some form of wicking action. The water transport in the flow fields was different than expected. The flow pattern looks like wavy-stratified flow not slug flow. Water waves move along the bottom of the cathode flow field. The waves are pushed along via friction with the moving air but their velocity is much lower than that of the air. Water drops form on the anode and cathode, and are removed from the surface probably by lift forces.

Water diffusion and capillary backpressure from the cathode GDL was found to be greater than electroosmotic drag at $200\,\mathrm{mA\,cm^{-2}}$. This was determined due to the increasing water content in the anode gas stream, as it traversed the anode flow field. It should be noted that the balance of forces between electroosmosis and diffusion are strongly dependent on operating current, and this result may change as operating current changes.

Acknowledgements

References

[1] P.P.K. Berg, J. St. Pierre, J. Stumper, B. Wetton, J. Electrochem. Soc. 151 (3) (2004) A341–A353.
[2] B. Uwe, S.J.C. Cleghorn, W.B. Johnson, Challenges PEM Fuel Cell Membr. (2005) 1103–1112.
[3] D. Cheddie, N. Munroe, J. Power Sources 147 (1–2) (2005) 72–84.
[4] L. Ma, D.B. Ingham, M. Pourkashanian, E. Carcadea, J. Fuel Cell Sci. Technol. 2 (4) (2005) 246–257.
[5] C.Y. Wang, Chem. Rev. 104 (10) (2004) 4727–4766.
[6] M.A. Hickner, N.P. Siegel, K.S. Chen, D.N. McBrayer, D.S. Hussey, D.L. Jacobson, M. Arif, J. Electrochem. Soc. 153 (5) (2006) A902–A908.
[7] D. Kramer, E. Lehmann, G. Frei, P. Vontobel, A. Wokaun, G.G. Scherer, Nucl. Instrum. Methods Phys. Res. Sec. A 542 (1–3) (2005) 52–60.
[8] D. Kramer, J.B. Zhang, R. Shimoi, E. Lehmann, A. Wokaun, K. Shinohara, G.G. Scherer, Electrochim. Acta 50 (13) (2005) 2603–2614.
[9] R. Satija, D.L. Jacobson, M. Arif, S.A. Werner, J. Power Sources 129 (2) (2004) 238–245.
[10] R.J. Bellows, M.Y. Lin, M. Arif, A.K. Thompson, D. Jacobson, J. Electrochem. Soc. 146 (3) (1999) 1099–1103.
[11] N. Pekula, K. Heller, P.A. Chuang, A. Turhan, M.M. Mench, J.S. Brenizer, K. Unlu, Nucl. Instrum. Methods Phys. Res. Sec. A 542 (1–3) (2005) 134–141.
[12] J.R.P. Jayakody, S.H. Chung, L. Durantino, H. Zhang, L. Xiao, B.C. Benicewicz, S.G. Greenbaum, J. Electrochem. Soc. 154 (2) (2007) B242–B246.
[13] S. Licoccia, M.L. Di Vona, A. D'Epifanio, D. Marani, M. Vittadello, J.R.P. Jayakody, S.G. Greenbaum, J. Electrochem. Soc. 153 (6) (2006) A1226–A1231.
[14] J.R.P. Jayakody, A. Khalfan, E.S. Mananga, S.G. Greenbaum, T.D. Dang, R. Mantz, J. Power Sources 156 (2) (2006) 195–199.
[15] K.W. Feindel, S.H. Bergens, R.E. Wasylishen, Chemphyschem 7 (1) (2006) 67–75.
[16] A.S. Arico, V. Baglio, V. Antonucci, I. Nicotera, C. Oliviero, L. Coppola, P.L. Antonucci, J. Membr. Sci. 270 (1–2) (2006) 221–227.
[17] S. Tsushima, K. Teranishi, K. Nishida, S. Hirai, Magn. Reson. Imaging 23 (2 Special Issue SI) (2005) 255–258.
[18] K. Teranishi, S. Tsushima, S. Hirai, Electrochem. Solid-State Lett. 8 (6) (2005) A281–A284.
[19] Y.J. Kim, B.R. Einsla, C.N. Tchatchoua, J.E. McGrath, High Perform. Polym. 17 (3) (2005) 377–401.
[20] D.S. Kim, H.B. Park, J.Y. Jang, Y.M. Lee, J. Polym. Sci. Part A-Polym. Chem. 43 (22) (2005) 5620–5631.
[21] H.A. Every, M.A. Hickner, J.E. McGrath, T.A. Zawodzinski, J. Membr. Sci. 250 (1–2) (2005) 183–188.
[22] M.G. Compton, K.C. Maynes, J. Pavelites, D.B. Baker, Solid State Commun. 136 (3) (2005) 138–141.
[23] S. Tsushima, K. Teranishi, S. Hirai, Electrochem. Solid State Lett. 7 (9) (2004) A269–A272.
[24] I. Fischbach, H.W. Spiess, K. Saalwachter, G.R. Goward, J. Phys. Chem. B 108 (48) (2004) 18500–18508.
[25] X.M. Ren, T.E. Springer, T.A. Zawodzinski, S. Gottesfeld, J. Electrochem. Soc. 147 (2) (2000) 466–474.
[26] J.J. Fontanella, M.C. Wintersgill, R.S. Chen, Y. Wu, S.G. Greenbaum, Electrochim. Acta 40 (13–14) (1995) 2321–2326.
[27] V.V. Binsu, R.K. Nagarale, V.K. Shahi, P.K. Ghosh, React. Funct. Polym. 66 (12) (2006) 1619–1629.
[28] C.N. Kostelansky, J.J. Pietron, M.S. Chen, W.J. Dressick, K.E. Swider-Lyons, D.E. Ramaker, R.M. Stroud, C.A. Klug, B.S. Zelakiewicz, T.L. Schull, J. Phys. Chem. B 110 (43) (2006) 21487–21496.
[29] Y. Daiko, L.C. Klein, T. Kasuga, M. Nogami, J. Membr. Sci. 281 (1–2) (2006) 619–625.
[30] T. Uma, A. Nakao, M. Nogami, Mater. Res. Bull. 41 (4) (2006) 817–824.
[31] J. Healy, C. Hayden, T. Xie, K. Olson, R. Waldo, A. Brundage, H. Gasteiger, J. Abbott, Fuel Cells 5 (2) (2005) 302–308.
[32] A. Noda, A.B. Susan, K. Kudo, S. Mitsushima, K. Hayamizu, M. Watanabe, J. Phys. Chem. B 107 (17) (2003) 4024–4033.

[33] J.D. Halla, M. Mamak, D.E. Williams, G.A. Ozin, Adv. Funct. Mater. 13 (2) (2003) 133–138.

[34] R. Guilard, S. Brandes, C. Tardieux, A. Tabard, M. Lher, C. Miry, P. Gouerec, Y. Knop, J.P. Collman, J. Am. Chem. Soc. 117 (47) (1995) 11721–11729.

[35] K.W. Feindel, L.P.A. LaRocque, D. Starke, S.H. Bergens, R.E. Wasylishen, J. Am. Chem. Soc. 126 (37) (2004) 11436–11437.

[36] K. Teranishi, S. Tsushima, S. Hirai, Electrochem. Solid State Lett. 8 (6) (2005) A281–A284.

[37] K. Teranishi, S. Tsushima, S. Hirai, J. Electrochem. Soc. 153 (4) (2006) A664–A668.

[38] S. Tsushima, K. Teranishi, K. Nishida, S. Hirai, Magn. Reson. Imaging 23 (2) (2005) 255–258.

[39] K.R. Minard, V.V. Viswanathan, P.D. Majors, L.Q. Wang, P.C. Rieke, J. Power Sources 161 (2) (2006) 856–863.

[40] M.S. Wilson, S. Gottesfeld, J. Appl. Electrochem. (1992) 22.

[41] T.J. Hanratty, Hershman, AIChE J. 7 (1962) 488–497.

[42] M.K. Akbar, S.M. Ghiaasiaan, Exp. Therm. Fluid Sci. 28 (1) (2003) 17–21.

[43] G.B. Wallis, J.E. Dodson, Int. J. Multiphase Flow 1 (1) (1973) 173–193.